Journal of Solid Mechanics Vol. 7, No. 3 (2015) pp. 344-363

On the Magneto-Thermo-Elastic Behavior of a Functionally Graded Cylindrical Shell with Pyroelectric Layers Featuring Interlaminar Bonding Imperfections Rested in an Elastic Foundation

M. Saadatfar* , M. Aghaie-Khafri

Faculty of Mechanical Engineering, K.N. Toosi University of Technology, Postal Code: 1999143344, Tehran, Iran

Received 29 June 2015; accepted 28 August 2015

ABSTRACT

The behavior of an exponentially graded hybrid cylindrical shell subjected to an axisymmetric thermo-electro-mechanical loading placed in a constant magnetic field is investigated. The hybrid shell is consisted of a functionally graded host layer embedded with pyroelectric layers as sensor and/or actuator that can be imperfectly bonded to the inner and the outer surfaces of a shell. The shell is simply supported and could be rested on an elastic foundation. The material properties of the host layer are assumed to be exponentially graded in the radial direction. To solve governing differential equations, the Fourier series expansion method along the longitudinal direction and the differential quadrature method (DQM) across the thickness direction are used. Numerical examples are presented to discuss effective parameters influence on the response of the hybrid shell.

Keywords : Pyroelectric ; Magnetic field ; Imperfect bonding ; Exponentially graded cylindrical shell ; Elastic foundation.

1 INTRODUCTION

FUNCTIONALLY graded material (FGM) is a class of inhomogeneous composite materials at a microscopic scale, which are widely studied and used in various industrial applications [1]. On the other hand, the coupling nature of piezoelectric materials are considered in electro-mechanical and electrical devices, such as actuators, sensors and transducers [2-4]. When the host structure is integrated with the piezoelectric layers, the integrity has the ability of sensing and actuating and is named as smart structures. In order to improve the performance and reliability of the smart structures, it is necessary to know exactly the mechanical behavior. Thus, many investigations were carried out in the subject area in the last decade [5-13]. In addition, investigation of the behavior of smart structures in multiphysics environment is essential for several applications concerning structural health monitoring, energy harvesting and green energy production, space vehicles, and self-powered biomedical devices [14]. The static and free vibration of FGM cylindrical shell bonded to a piezoelectric layer is analyzed by Alibeigloo et al. [15, 16]. Furthermore, the coupled interaction of physical phenomena involve elastic, electric, and thermal fields in multiphysics behavior of smart layered cylindrical composites is investigated by many researchers. Alibeigloo [17, 18] provided a thermo-elastic solution for deformations of a simply-supported FGM cylindrical shell and panel

* Corresponding author. Tel.: +98 912 3088389; Fax: +98 21 88674748.
E-mail address: maghaei@kntu.ac.ir (M. Aghaei-Khafri).

bonded to piezoelectric layers. Akbari Alashti and Khorsand [19, 20] carried out static and dynamic analysis of FGM cylindrical shells with piezoelectric layers under thermo-electro-mechanical loads, using the DQ method. Multiphysics analysis behavior of FGMs are very important due to their many applications in magnetic storage elements, plasma physics and the corresponding measurement methods of magneto-thermo-elasticity. Ghorbanpour et al [21-23] studied the magnetothermoelastic interactions in cylindrical and spherical FGM and piezoelectric structures. Thermo-magneto-dynamic stresses in a non-homogeneous hollow cylinder was investigated by Kong et al [24]. Analysis on the effect of centrifugal load in FGM hollow sphere subjected to a magnetic field is carried out by Khalili et. al. [25]. Recently, the electromagnetoelastic behavior of a FGPM hollow cylinder under multifield loading was analyzed [26].Imperfect interfacial bonding or delamination is an ordinary type of flaw in laminated composite structures owing to manufacturing defects or environmental conditions. This becomes more significant in hybrid laminates because of high transverse stresses developed at elastic-piezoelectric interfaces under electric potential loading.The actuation/sensing authority of smart layers may extensively be affected due to the imperfection at the interfaces. Furthermore, analyzing composite structures on elastic foundations has always attracted the attention of both researchers and engineers [27-33]. Concerning the application of smart composite structures under different environmental conditions, it is vital to analyse the effect of imperfect bonding and elastic foundations for an accurate prediction of the structural behavior.Regarding the application of smart composite structures under different external loadings and various environmental conditions, Saadatfar and Aghaie-Khafri [34] presented analytical solution for the multiphysics magneto-thermo-electro-elastic problem of a long FGM hollow cylinder bonded to smart layers. To the best of the authors' knowledge, however, the electro-magneto-thermo-elastic analysis of an exponentially graded cylindrical shell imperfectly bonded with pyroelectric layers resting on an elastic foundation has not yet been reported.

In the present study, a simply supported FGM cylindrical shell with surface bounded pyroelectric layers as sensor and/or actuator under pressure, electrical excitation, thermal condition where placed in a constant magnetic field is studied. The material properties of the FGM shell are assumed to be exponentially graded in the radial direction. The highly coupled partial differential equations are reduced to ordinary differential equations with variable coefficients by means of trigonometric function expansion in the longitudinal directions. Then, the DQ method is used across the thickness direction to solve the resulting equations. Numerical examples are given to reveal the impact of effective parameters on the behavior of a FG smart cylindrical shell.

2 BASIC EQUATIONS

As it is shown in Fig. 1, an axisymmetric FGM shell with inner and outer surfaces bonded to pyroelectric layers is considered. Owing to the symmetry of the shell geometry and the boundary conditions, the thermal, mechanical and electrical fields are assumed to be independent of the circumferential coordinate. The shell material is assumed to be FGM and isotropic. Besides, the pyroelectric material is assumed to be transversely isotropic and the radial direction is the axis of the transverse isotropy.

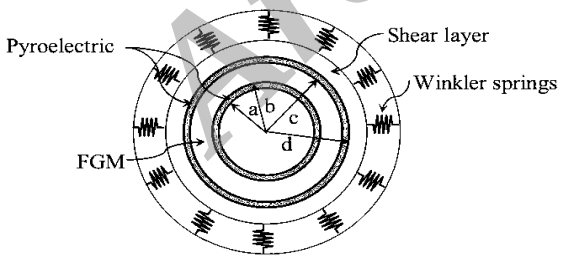

Fig.1
FGM hollow cylinder with pyroelectric layers resting on an elastic foundation.

2.1 Heat conduction problem

A steady state heat conduction without internal heat source is considered and the governing equations of the steady state temperature field for FGM and pyroelectric layers are [17]:

$$\frac{1}{r}\frac{\partial}{\partial r}\left(rk_m\frac{\partial T_f}{\partial r}\right)+\frac{\partial}{\partial z}\left(k_m\frac{\partial T_f}{\partial z}\right)=0 \tag{1a}$$

$$\frac{k_{rp}}{r}\frac{\partial}{\partial r}\left(r\frac{\partial T_p}{\partial r}\right)+k_{zp}\frac{\partial^2 T_p}{\partial z^2}=0 \tag{1b}$$

where k_{rp} and k_{zp} are the thermal conductivity of the pyroelectric in the radial and longitudinal directions and k_f is the thermal conductivity of FGM layer. T_f and T_p denote the temperature distribution of the FGM layer and the piezoelectric layer, respectively. The thermal boundary conditions are:

$$\begin{aligned} &T_j(r,0)=T_j(r,L)=0, \quad j=i,f,o \\ &T_i(a,z)=T_a, \quad T_o(d,z)=0, \end{aligned} \tag{2}$$

The solution of the thermal problem is governed by Eqs. (1-2) and satisfies temperature boundary conditions at the end faces as:

$$T_j=\sum_{n=1}^{\infty}\bar{T}_{jn}(r)\sin(p_n z), \qquad j=i,f,o \tag{3}$$

where $p_n=\frac{n\pi}{L}$ The exponential law is assumed for the thermal conductivity constant, Young's modulus, magnetic permeability and the coefficient of the thermal expansion of FGM as:

$$E=E_f e^{\eta_1(r-b)}, \quad \alpha=\alpha_f e^{\eta_2(r-b)}, \quad \mu=\mu_f e^{\eta_3(r-b)}, \quad k_m=k_f e^{\eta_4(r-b)}, \tag{4}$$

where subscript *f* denotes the material properties in the inner surface of the FGM layer and η_i are their grading parameters. Poisson's ratio (ν) is taken to be constant through the shell thickness. Using Eqs. (3, 4), the Eqs. (1) are obtained as:

$$\left(\frac{1}{r}+\eta_4\right)\frac{d\bar{T}_f}{dr}+\frac{d^2\bar{T}_f}{dr^2}-p_n^2\bar{T}_f=0, \tag{5a}$$

$$k_{rp}\left(\frac{1}{r}\frac{d\bar{T}_p}{dr}+\frac{d^2\bar{T}_p}{dr^2}\right)-k_{zp}p_n^2\bar{T}_p=0, \tag{5b}$$

2.2 FGM layer

The following relations are used to express the stresses in the shell [17]:

$$\begin{aligned} \sigma_r &= \frac{E(r)}{(1+\nu)(1-2\nu)}\left[(1-\nu)\varepsilon_r+\nu\varepsilon_\theta+\nu\varepsilon_z\right]-\frac{\alpha(r)E(r)}{1-2\nu}T(r,z) \\ \sigma_\theta &= \frac{E(r)}{(1+\nu)(1-2\nu)}\left[\nu\varepsilon_r+(1-\nu)\varepsilon_\theta+\nu\varepsilon_z\right]-\frac{\alpha(r)E(r)}{1-2\nu}T(r,z) \\ \sigma_z &= \frac{E(r)}{(1+\nu)(1-2\nu)}\left[\nu\varepsilon_r+\nu\varepsilon_\theta+(1-\nu)\varepsilon_z\right]-\frac{\alpha(r)E(r)}{1-2\nu}T(r,z) \\ \tau_{zr} &= \frac{E(r)}{2(1+\nu)}\gamma_{zr} \end{aligned} \tag{6}$$

The strain-displacement relations are defined as [17]:

$$\varepsilon_r = \frac{\partial u_r}{\partial r}, \varepsilon_\theta = \frac{u_r}{r}, \varepsilon_z = \frac{\partial u_z}{\partial z}, \quad \gamma_{zr} = \left(\frac{\partial u_r}{\partial z} + \frac{\partial u_z}{\partial r} \right) \tag{7}$$

The shell is placed initially in an axial constant magnetic field. There is an interaction between deformation and perturbation of the magnetic field vector in the shell. Omitting displacement electric currents, the governing electrodynamic Maxwell equations for a perfectly conducting elastic body are given by [35]:

$$\vec{J} = \nabla \times \vec{h}, \qquad \nabla \times \vec{e} = -\mu \frac{\partial \vec{h}}{\partial t}, \qquad div\ \vec{h} = 0, \qquad \vec{e} = -\mu \left(\vec{U} \frac{\partial \vec{U}}{\partial t} \times \vec{H} \right), \qquad \vec{h} = \nabla \times (\vec{U} \times \vec{H}), \tag{8}$$

where, $\vec{U}, \vec{H}, \vec{h}$ are displacement vector, magnetic intensity vector and perturbation of the magnetic field vector, respectively. Equilibrium equations for axisymmetric deformations of the shell by taking into account the Lorentz force are written as [19, 24]:

$$\begin{aligned} &\frac{\partial \sigma_r}{\partial r} + \frac{\partial \tau_{rz}}{\partial z} + \frac{\sigma_r - \sigma_\theta}{r} + f_r = 0 \\ &\frac{\partial \tau_{rz}}{\partial r} + \frac{\partial \sigma_z}{\partial z} + \frac{\tau_{rz}}{r} = 0 \end{aligned} \tag{9}$$

where f_r is defined as the Lorentz's force. By applying an initial magnetic field vector in the cylindrical coordinate system to Eq. (8), the Lorentz's force is:

$$f_r = \mu(\vec{J} \times \vec{H}) = \mu H^2 \left(\frac{\partial^2 u_r}{\partial z^2} + \frac{1}{r} \frac{\partial u_r}{\partial r} - \frac{u_r}{r^2} + \frac{\partial^2 u_r}{\partial r^2} \right) \tag{10}$$

Using Eq. (10) and Eq. (6) , Eq. (9) can be rewritten as:

$$\begin{aligned} &\frac{1}{(1+\nu)(1-2\nu)} \left(\left\{ E \left[(1-\nu) \left(\frac{\partial^2}{\partial r^2} + \frac{1}{r} \frac{\partial}{\partial r} - \frac{1}{r^2} \right) \right] + \frac{\partial E}{\partial r} \left[(1-\nu) \frac{\partial}{\partial r} + \frac{\nu}{r} \right] + \frac{E(1-2\nu)}{2} \left[\frac{\partial}{\partial z^2} \right] \right\} u_r \right. \\ &\left. + \left\{ \frac{E}{2} \frac{\partial^2}{\partial r \partial z} + \nu \frac{\partial E}{\partial r} \frac{\partial}{\partial z} \right\} u_z \right) + \mu H^2 \left(\frac{\partial^2 u_r}{\partial z^2} + \frac{1}{r} \frac{\partial u_r}{\partial r} - \frac{u_r}{r^2} + \frac{\partial^2 u_r}{\partial r^2} \right) - \frac{1}{1-2\nu} \left(\frac{d\alpha}{dr} E T_f + \frac{dE}{dr} \alpha T_f + E\alpha \frac{\partial T_f}{\partial r} \right) = 0 \end{aligned} \tag{11a}$$

$$\begin{aligned} &\frac{1}{2(1+\nu)} \left(\left\{ \frac{E}{1-2\nu} \frac{\partial^2}{\partial r \partial z} + \left(\frac{E}{(1-2\nu)r} + \frac{1}{r} \frac{\partial E}{\partial r} \right) \frac{\partial}{\partial z} \right\} U_r \right. \\ &\left. + \left\{ \frac{2E}{(1-2\nu)} \left[(1-\nu) \frac{\partial^2}{\partial z^2} \right] + E \left[\frac{\partial^2}{\partial r^2} \right] + \left[\frac{E}{r} + \frac{1}{r} \frac{\partial E}{\partial r} \right] \frac{\partial}{\partial r} \right\} U_z \right) - \frac{\alpha E}{1-2\nu} \frac{\partial T_f}{\partial z} = 0 \end{aligned} \tag{11b}$$

2.3 Pyroelectric layers

The constitutive equations of a pyroelectric material in cylindrical coordinate can be expressed as [17]:

$$\begin{aligned}
\sigma_r &= c_{11}\varepsilon_r + c_{12}\varepsilon_\theta + c_{13}\varepsilon_z - e_{11}E_r - \lambda_r T \\
\sigma_\theta &= c_{12}\varepsilon_r + c_{22}\varepsilon_\theta + c_{23}\varepsilon_z - e_{21}E_r - \lambda_\theta T \\
\sigma_z &= c_{13}\varepsilon_r + c_{23}\varepsilon_\theta + c_{33}\varepsilon_z - e_{31}E_r - \lambda_z T \\
\tau_{rz} &= c_{55}\gamma_{zr} - e_{53}E_z \\
D_r &= e_{11}\varepsilon_r + e_{21}\varepsilon_\theta + e_{31}\varepsilon_z + g_{11}E_r + P_1 T \\
D_z &= e_{53}\gamma_{zr} + g_{33}E_z
\end{aligned} \tag{12}$$

where σ_i, ε_i, D_i and E_i represent stress, strain, electric displacement and electric fields, respectively. C_{ij}, e_{ij} and g_{ij} denote the elastic, piezoelectric and dielectric constants, respectively. λ_i and P_i are the thermal modulus and pyroelectric constants, respectively. T expresses the temperature variation in the pyroelectric layer and λ_i are [26]:

$$\begin{aligned}
\lambda_r &= c_{11}\alpha_r + c_{12}\alpha_\theta + c_{13}\alpha_z \\
\lambda_\theta &= c_{12}\alpha_r + c_{22}\alpha_\theta + c_{23}\alpha_z \\
\lambda_z &= c_{13}\alpha_r + c_{23}\alpha_\theta + c_{33}\alpha_z
\end{aligned} \tag{13}$$

Considering the electric potential ψ, the electric field E, is given by [17, 19]:

$$E_r = -\frac{\partial \psi}{\partial r}, \qquad E_z = -\frac{\partial \psi}{\partial z} \tag{14}$$

For the pyroelectric layers, the equation of the electrostatic charge is [17]:

$$\frac{1}{r}\frac{\partial}{\partial r}\left(rD_r\right) + \frac{\partial D_z}{\partial z} = 0 \tag{15}$$

Using Eqs. (12), (14) and (10), Eqs. (9) and (15) can be written as:

$$\begin{aligned}
&\left(c_{11}\frac{\partial^2}{\partial r^2} + \frac{c_{11}}{r}\frac{\partial}{\partial r} + -\frac{c_{22}}{r^2} + c_{55}\frac{\partial^2}{\partial z^2}\right)u_r + \left(\left(\frac{c_{13}-c_{23}}{r}\right)\frac{\partial}{\partial z} + \left(c_{13}+c_{55}\right)\frac{\partial}{\partial r \partial z}\right)u_z \\
&+\left(e_{11}\frac{\partial^2}{\partial r^2} + \left(\frac{e_{11}-e_{21}}{r}\right)\frac{\partial}{\partial r} + e_{53}\frac{\partial^2}{\partial z^2}\right)\psi + \mu H^2\left(\frac{\partial^2 u_r}{\partial z^2} + \frac{1}{r}\frac{\partial u_r}{\partial r} - \frac{u_r}{r^2} + \frac{\partial^2 u_r}{\partial r^2}\right) + \left(\frac{1}{r}\left(\lambda_\theta - \lambda_r\right) - \lambda_r\frac{\partial}{\partial r}\right)T = 0
\end{aligned} \tag{16a}$$

$$\begin{aligned}
&\left(\left(\frac{c_{55}+c_{23}}{r}\right)\frac{\partial}{\partial z} + \left(c_{55}+c_{13}\right)\frac{\partial}{\partial r \partial z}\right)u_r + \left(\frac{c_{55}}{r}\frac{\partial}{\partial r} + c_{55}\frac{\partial^2}{\partial r^2} + c_{33}\frac{\partial^2}{\partial z^2}\right)u_z \\
&+\left(\frac{e_{53}}{r}\frac{\partial}{\partial z} + \left(e_{53}+e_{31}\right)\frac{\partial}{\partial r \partial z}\right)\psi - \lambda_z\frac{\partial}{\partial z}T_p = 0
\end{aligned} \tag{16b}$$

$$\begin{aligned}
&\left(\frac{e_{11}+e_{21}}{r}\frac{\partial}{\partial r} + e_{11}\frac{\partial^2}{\partial r^2} + e_{53}\frac{\partial^2}{\partial z^2}\right)u_r + \left(\left(e_{53}+e_{31}\right)\frac{\partial}{\partial r \partial z} + \frac{e_{31}}{r}\frac{\partial}{\partial z}\right)u_z \\
&-\left(\frac{g_{11}}{r}\frac{\partial}{\partial r} + g_{11}\frac{\partial^2}{\partial r^2} + g_{33}\frac{\partial^2}{\partial z^2}\right)\psi + P_1\left(\frac{1}{r} + \frac{\partial}{\partial r}\right)T = 0
\end{aligned} \tag{16c}$$

The simply supported boundary conditions are [17]:

$$u_r = \sigma_z = \psi = 0 \quad at\ z = 0, L \tag{17}$$

Since the outer surface of the hybrid shell is assumed to be subjected to a Winkler-Pasternak elastic foundation, the surface boundary conditions can be considered as [36]:

$$\begin{aligned} &\sigma_r = -p, \quad \tau_{zr} = 0, \quad \psi = V, \qquad at\ r = a \\ &\sigma_r = -\left[K_L u_r - K_S \left(\frac{\partial^2 u_r}{\partial r^2} + \frac{1}{r}\frac{\partial u_r}{\partial r} + \frac{\partial^2 u_r}{\partial z^2} \right) \right], \ \tau_{zr} = 0, \qquad D_r = 0, \qquad at\ r = d \end{aligned} \tag{18}$$

where Winkler spring stiffness and shear layer stiffness are indicated by K_L and K_S.

For the imperfect interfaces, the displacements as well as the temperature field at the interfaces may be discontinuous. However, the tractions at the interfaces and the heat flux are always continuous. The continuity conditions that must be met at interfaces of all the adjacent layers between k_{th} and $(k+1)_{th}$ interfaces are expressed as following [19]:

$$\sigma_r\big|_{k+1} = \sigma_r\big|_k, \qquad \tau_{rz}\big|_{k+1} = \tau_{rz}\big|_k, \qquad \psi\big|_{k+1} = \psi\big|_k, \qquad k_r \frac{\partial T}{\partial r}\bigg|_{k+1} = k_r \frac{\partial T}{\partial r}\bigg|_k, \qquad at\ r = b, c \tag{19}$$

The linear spring model is considered for the displacement field and thermal field discontinuity is assumed. According to this model, the discontinuities in the displacements and temperature at the interfaces are proportional to their respective traction components and transverse rate of the heat flow. These discontinuity conditions are [37]:

$$\begin{aligned} &u_r\big|_{k+1} - u_r\big|_k = \chi_r^k \sigma_r, \\ &u_z\big|_{k+1} - u_z\big|_k = \chi_z^k \tau_{rz}, \\ &T_{k+1} - T_k = \chi_T^k\, k_r \frac{\partial T}{\partial r}\bigg|_{k+1} \qquad k = 1,2 \ \ at\ r = b, c \end{aligned} \tag{20}$$

where χ_i^k are the compliance constants of inner and outer interfaces for displacements and thermal field. It is clear that for a perfectly bonded interface we have $\chi_i^k = 0\ (k = 1,2)$. A non-zero normal compliance coefficient χ_r^k, characterizes the normal opening delamination, whereas the shear slip delamination is characterized by non-zero tangential compliance coefficients χ_z^k. For the normal opening delamination mode, the normal stresses at interfaces should not be negative to allow no material penetration. The thermal imperfections are just applicable when a normal opening delamination is present ($\chi_r^k \neq 0$).

3 SOLUTION OF GOVERNING DIFFERENTIAL EQUATION

The solution satisfying the boundary conditions may be assumed as:

$$u_r = \sum_{n=1}^{\infty} U_r(r)\sin(b_n z), \qquad u_z = \sum_{n=1}^{\infty} U_z(r)\cos(b_n z), \qquad \psi = \sum_{n=1}^{\infty} \Psi(r)\sin(b_n z) \tag{21}$$

where $b_n = \frac{n\pi}{L}$. Substituting Eq. (21) into governing equations, partial differential equations reduce to ordinary differential equations and governing equations for the FGM shell can be expressed as:

$$\frac{1}{(1+\nu)(1-2\nu)}\left(\left\{E\left[(1-\nu)\left(\frac{d^2}{dr^2}+\frac{1}{r}\frac{d}{dr}-\frac{1}{r^2}\right)\right]+\frac{\partial E}{\partial r}\left[(1-\nu)\frac{d}{dr}+\frac{\nu}{r}\right]\right.\right.$$
$$\left.+\frac{E(1-2\nu)}{2}\left[-b_n^2\right]+(1+\nu)(1-2\nu)\mu H^2\left(-b_n^2+\frac{1}{r}\frac{d}{dr}-\frac{1}{r^2}+\frac{d^2}{dr^2}\right)\right\}U_r \quad (22a)$$
$$\left.+\left\{-\frac{Eb_n}{2}\frac{d}{dr}-\nu\frac{\partial E}{\partial r}b_n\right\}U_z\right)-\frac{1}{1-2\nu}\left(\frac{d\alpha}{dr}E\bar{T}+\frac{dE}{dr}\alpha\bar{T}+E\alpha\frac{d\bar{T}}{dr}\right)=0$$

$$\frac{1}{2(1+\nu)}\left(\left\{\frac{Eb_n}{1-2\nu}\frac{d}{dr}+\left(\frac{E}{(1-2\nu)r}+\frac{1}{r}\frac{\partial E}{\partial r}\right)b_n\right\}U_r\right.$$
$$\left.+\left\{\frac{-2E}{(1-2\nu)}\left[(1-\nu)b_n^2\right]+E\left[\frac{d^2}{dr^2}\right]+\left[\frac{E}{r}+\frac{1}{r}\frac{\partial E}{\partial r}\right]\frac{d}{dr}\right\}U_z\right)-\frac{\alpha Eb_n}{1-2\nu}\bar{T}=0 \quad (22b)$$

and corresponding equations for the pyroelectric layers can be expressed as:

$$\left\{\left(c_{11}\frac{d^2}{dr^2}+\frac{c_{11}}{r}\frac{d}{dr}+\frac{c_{12}}{r}-\frac{c_{22}}{r^2}-c_{55}b_n^2+\mu H^2\left(-b_n^2+\frac{1}{r}\frac{d}{dr}-\frac{1}{r^2}+\frac{d^2}{dr^2}\right)\right)U_r\right.$$
$$\left.-\left(b_n\left(\frac{c_{13}-c_{23}}{r}\right)+b_n(c_{13}+c_{55})\frac{d}{dr}\right)U_z+\left(e_{11}\frac{d^2}{dr^2}+\left(\left(\frac{e_{11}-e_{21}}{r}\right)\frac{d}{dr}\right)-e_{53}b_n^2\right)\Psi\right\}+\left(\frac{1}{r}(\lambda_\theta-\lambda_r)-\lambda_r\frac{d}{dr}\right)\bar{T}=0 \quad (23a)$$

$$\left\{\left(b_n\left(\frac{c_{55}+c_{23}}{r}\right)+b_n(c_{55}+c_{13})\frac{d}{dr}\right)U_r+\left(\frac{c_{55}}{r}\frac{d}{dr}+c_{55}\frac{d^2}{dr^2}-c_{33}b_n^2\right)U_z\right.$$
$$\left.+\left(\frac{b_ne_{53}}{r}+b_n(e_{53}+e_{31})\frac{d}{dr}\right)\Psi\right\}-\lambda_z b_n\bar{T}=0 \quad (23b)$$

$$\left\{\left(\frac{e_{11}+e_{21}}{r}\frac{d}{dr}+e_{11}\frac{d^2}{dr^2}-e_{53}b_n^2\right)U_r-\left(b_n(e_{53}+e_{31})\frac{d}{dr}+\frac{b_ne_{31}}{r}\right)U_z\right.$$
$$\left.-\left(\frac{g_{11}}{r}\frac{d}{dr}+g_{11}\frac{d^2}{dr^2}-g_{33}b_n^2\right)\Psi\right\}+P_1\left(\frac{1}{r}+\frac{d}{dr}\right)\bar{T}=0 \quad (23c)$$

According to the DQM, the n_{th}-order derivative of the function *f(r)* at any sample point can be approximated by the following formulation [38]:

$$\frac{d^n f(r_i)}{dr^n}=\sum_{j=1}^{N}A_{ij}^{(n)}f(r_j) \qquad i=1\ldots\ldots N \quad n=1\ldots\ldots N-1 \quad (24)$$

where A_{ij} are the weighting coefficients associate with the n_{th}-order derivatives, and *N* is the number of grid points in the *r* direction. The weighting coefficients can be determined as [38]:

$$
\begin{aligned}
A_{ij}^{(1)} &= \frac{\Pi(r_i)}{(r_i - r_j).\Pi(r_j)} && i, j = 1,\ldots,N \ \ and \ \ j \neq i \\
A_{ij}^{(2)} &= 2\left[A_{ii}^{(1)} A_{ij}^{(1)} - \frac{A_{ij}^{(1)}}{r_i - r_j}\right] && 2 \le n \le N-1 \\
A_{ii}^{(1)} &= -\sum_{\mathrm{j=1\,j\neq i}}^{N} A_{ij}^{(1)} && k = 1,\ldots,N-1 \\
\Pi(r_i) &= \prod_{\mathrm{j=1\,j\neq i}}^{\mathrm{N}} (r_i - r_j)
\end{aligned}
\tag{25}
$$

For numerical computation, the Chebyshev–Gauss–Lobatto points with the following coordinates are used [38]:

$$
r_i = \frac{L}{2}\left(1 - \cos\left[\frac{(i-1)\pi}{(N-1)}\right]\right) \quad i = 1,2,3,\ldots,N \tag{26}
$$

Using the DQ technique, the equations of the FGM layer, PYROELECTRIC layers and thermal field can be expressed as:

FGM layer:

$$
\begin{aligned}
&\frac{E_f e^{\eta_1(r_i-b)}}{(1+\nu)(1-2\nu)}\left(\left\{\left[(1-\nu)\left(\sum_{j=1}^{N} B_{ij}^{(2)} + \frac{1}{r_i}\sum_{j=1}^{N} B_{ij}^{(1)} - \frac{1}{r_i^{\,2}}\right)\right] + \eta_1\left[(1-\nu)\sum_{j=1}^{N} B_{ij}^{(1)} + \frac{\nu}{r_i}\right]\right.\right. \\
&\left.\left. -\frac{(1-2\nu)}{2} b_n^2 + \frac{(1+\nu)(1-2\nu)}{E_f}\mu_f H^2 e^{(\eta_3-\eta_1)(r_i-b)}\left(-b_n^2 + \sum_{j=1}^{N} B_{ij}^{(2)} + \frac{1}{r_i}\sum_{j=1}^{N} B_{ij}^{(1)} - \frac{1}{r_i^{\,2}}\right)\right\} U_{rj}\right. \\
&\left. + \left\{-\frac{b_n}{2}\sum_{j=1}^{N} B_{ij}^{(1)} - \nu\eta_1 b_n\right\} U_{zj} - \frac{\alpha_0}{1-2\nu} e^{\eta_2(r_i-b)}\left(\eta_2 + \eta_1 + \sum_{j=1}^{N} B_{ij}^{(1)}\right)\bar{T}\right) = 0
\end{aligned}
\tag{27a}
$$

$$
\begin{aligned}
&\frac{E_f e^{\eta_1(r_i-b)}}{2(1+\nu)}\left(\left\{\frac{b_n}{1-2\nu}\sum_{j=1}^{N} B_{ij}^{(1)} + \frac{1}{r_i}\left(\frac{1}{(1-2\nu)} + \eta_1\right) b_n\right\} U_{rj}\right. \\
&\left. + \left\{\frac{-2}{(1-2\nu)}(1-\nu) b_n^2 + \sum_{j=1}^{N} B_{ij}^{(2)} + \frac{1}{r_i}(1+\eta_1)\sum_{j=1}^{N} B_{ij}^{(1)}\right\} U_{zj} - \frac{\alpha_f b_n}{1-2\nu} e^{\eta_2(r_i-b)}\bar{T}\right) = 0
\end{aligned}
\tag{27b}
$$

Pyroelectric layer:

$$
\begin{aligned}
&\left\{\left(\left(c_{11} + \mu H^2\right)\sum_{j=1}^{N} A_{ij}^{(2)} + \left(\frac{c_{11} + \mu H^2}{r_i}\right)\sum_{j=1}^{N} A_{ij}^{(1)} - \frac{c_{22} + \mu H^2}{r_i^{\,2}}\right.\right. \\
&\left.\left. -\left(c_{55} + \mu H^2\right) b_n^2\right) U_{rj} - \left(b_n\left(\frac{c_{13}}{r_i} - \frac{c_{23}}{r_i}\right) + b_n^2\left(c_{13} + c_{55}\right)\sum_{j=1}^{N} A_{ij}^{(1)}\right) U_{zj}\right. \\
&\left. + \left(e_{11}\sum_{j=1}^{N} A_{ij}^{(2)} + \left(\frac{e_{11}}{r_i} - \frac{e_{21}}{r_i}\right)\sum_{j=1}^{N} A_{ij}^{(1)} - e_{53} b_n^2\right)\Psi_j\right\} + \left(\frac{1}{r_i}\left(\lambda_\theta - \lambda_r\right) - \lambda_r \sum_{j=1}^{N} A_{ij}^{(1)}\right)\bar{T} = 0
\end{aligned}
\tag{28a}
$$

$$\left\{\left(b_n\left(\frac{c_{55}+c_{23}}{r_i}\right)+b_n\left(c_{55}+c_{13}\right)\sum_{j=1}^{N}A_{ij}^{(1)}\right)U_{rj}+\left(\frac{c_{55}}{r_i}\sum_{j=1}^{N}A_{ij}^{(1)}+c_{55}\sum_{j=1}^{N}A_{ij}^{(2)}-c_{33}b_n^2\right)U_{zj}\right.$$
$$\left.+\left(\frac{b_n e_{53}}{r_i}+b_n\left(e_{53}+e_{31}\right)\sum_{j=1}^{N}A_{ij}^{(1)}\right)\Psi_j-\lambda_z b_n\bar{T}\right\}=0 \tag{28b}$$

$$\left(\left(\frac{e_{11}+e_{21}}{r_i}\right)\sum_{j=1}^{N}A_{ij}^{(1)}+e_{11}\sum_{j=1}^{N}A_{ij}^{(2)}-e_{53}b_n^2\right)U_{rj}-\left(b_n\left(e_{53}+e_{31}\right)\sum_{j=1}^{N}A_{ij}^{(1)}+\frac{b_n e_{31}}{r_i}\right)U_{zj}$$
$$-\left(\frac{g_{11}}{r_i}\sum_{j=1}^{N}A_{ij}^{(1)}+g_{11}\sum_{j=1}^{N}A_{ij}^{(2)}-g_{33}b_n^2\right)\Psi_j+P_1\left(\frac{1}{r_i}+\sum_{j=1}^{N}A_{ij}^{(1)}\right)\bar{T}=0 \tag{28c}$$

Thermal field:

$$\left(k_{rp}\left(\frac{1}{r_i}\sum_{j=1}^{N}A_{ij}^{(1)}+\sum_{j=1}^{N}A_{ij}^{(2)}\right)-k_{zp}p_n^2\right)\bar{T}_i=0,\qquad\left(\left(\frac{1}{r_i}+\eta_4\right)\sum_{j=1}^{N}B_{ij}^{(1)}+\sum_{j=1}^{N}B_{ij}^{(2)}-p_n^2\right)\bar{T}_f=0, \tag{29}$$

In the above equations, A_{ij} and B_{ij} are weighting coefficients for pyroelectric and FGM layers, respectively. In a similar way, the boundary conditions can be discretized. So, the boundary conditions at $r=a$ and $r=d$ becomes:

$$\left[\left(c_{11}\sum_{j=1}^{N}A_{ij}^{(1)}+\frac{c_{12}}{a}\right)U_r-c_{13}b_nU_z+e_{11}\sum_{j=1}^{N}A_{ij}^{(1)}\Psi\right]-\lambda_r\bar{T}=-p,$$
$$\left[c_{55}\left(b_nU_r+\sum_{j=1}^{N}A_{ij}^{(1)}U_z\right)+e_{53}b_n\Psi\right]=0,\qquad\Psi=V, \tag{30}$$

$$\left[\left(c_{11}\sum_{j=1}^{N}A_{ij}^{(1)}+\frac{c_{12}}{d}-\left(K_LU_r\right)+K_S\left(\sum_{j=1}^{N}A_{ij}^{(2)}+\frac{1}{r}\sum_{j=1}^{N}A_{ij}^{(1)}-b_n^2\right)\right)U_r-c_{13}b_nU_z+e_{11}\sum_{j=1}^{N}A_{ij}^{(1)}\Psi\right]-\lambda_r\bar{T}=0$$
$$\left[c_{55}\left(b_nU_r+\sum_{j=1}^{N}A_{ij}^{(1)}U_z\right)+e_{53}b_n\Psi\right]=0,\quad\left[\left(e_{11}\sum_{j=1}^{N}A_{ij}^{(1)}+\frac{e_{21}}{d}\right)U_r-e_{31}b_nU_z-g_{11}\sum_{j=1}^{N}A_{ij}^{(1)}\Psi\right]+P_1\bar{T}=0, \tag{31}$$

Domain and boundary degrees of freedom are separated. In vector forms, they are denoted as (*d*) and (*b*), respectively. Based on this definition, the matrix form of governing equations and related boundary conditions take the following form:

$$\begin{bmatrix}[A_{bb}] & [A_{bd}]\\ [A_{db}] & [A_{dd}]\end{bmatrix}\begin{Bmatrix}\{U_b\}\\ \{U_d\}\end{Bmatrix}=\begin{Bmatrix}\{F_b\}\\ \{F_d\}\end{Bmatrix} \tag{32}$$

where,

$$\{U_b\}=\{\{U_{rb}\},\{U_{zb}\},\{\psi_b\}\}^T$$
$$\{U_d\}=\{\{U_{rd}\},\{U_{zd}\},\{\psi_d\}\}^T \tag{33}$$

It is worth mentioning that the grid point of each pyroelectric layer and FGM layer are considered as N_p and N_f. Thus, in the Eq. 32, the matrix dimension of the matrix A is $(2\times3N_p+2N_f)\times(2\times3\ N_p+2N_f)$ and the dimension of F and U is $(2\times3N_p+2N_f)\times1$. By eliminating the column vector $\{U_b\}$; the matrix Eq. (33) is reduced to the following system of algebraic equations:

$$[A]\{U_d\}=\{F\} \tag{34}$$

where,

$$\begin{aligned}[A]&=[A_{dd}]-[A_{db}][A_{bb}]^{-1}[A_{bd}]\\ \{F\}&=\{F_d\}-[A_{db}][A_{bb}]^{-1}\{F_b\}\end{aligned} \tag{35}$$

Eq. (34) is a system of algebraic equations which can be solved using various direct or iterative methods. As displacement vector is known, strains and stresses can be evaluated. Since, the size of resulting algebraic equations is large, the direct methods may not be efficient. The use of iterative methods, such as the Gauss–Seidel method, thus, is recommended for the solution of the resultant algebraic equations.

4 NUMERICAL RESULTS AND DISSCUTIONS

Considering numerical calculations, the FGM layer is assumed to be consisting of the inner surface made of Zirconia and the outer one made of Monel. Also, the pyroelectric layers is assumed to be $Ba_2NaNb_5O_{15}$ and PZT-4 that commonly used in the industry as actuator and sensor layers [17]. Material constants for pyroelectric layers are listed in Table 1. [17, 39] and the material constants of Zirconia and Monel are [19]:

$$\begin{aligned}&E_h=227.24(GPa), \quad \alpha_h=15\times10^{-6}(1/K), \quad k_h=25(W/mK)\\ &E_0=125.83(GPa), \quad \alpha_0=10\times10^{-6}(1/K), \quad k_0=2.09(W/mK)\end{aligned}$$

The material properties of the host shell are assumed to vary according to the exponential form and material property parameters η_1, η_2 and η_5 are:

$$\eta_1=\frac{\ln(E_h/E_0)}{c-b},\ \eta_2=\frac{\ln(\alpha_h/\alpha_0)}{c-b},\ \eta_4=\frac{\ln(k_h/k_0)}{c-b}$$

In the present work, $\eta_3=1$ is considered. It should be noted that 40 terms are considered in the series expansion and all numerical results are calculated and presented for the value of $z=L/2$. In all numerical simulations, unless otherwise stated, the values of $a=0.8\ m$, $d=1\ m$, $h_{FGM}=20\ h_{pyroelectric}$ and $L=6\ m$. Also, following dimensionless quantities are introduced:

$$R=\frac{r-a}{d-a},\quad u_i^*=\frac{u_i(r)}{h_{FGM}}\ (i=r,z),\quad \sigma_j^*=\frac{\sigma_j}{P_a},(j=r,\theta,z),\quad \tau_{rz}^*=\frac{\tau_{rz}}{P_a},\ T^*=\frac{T}{T_a}.$$

In order to demonstrate the convergence and accuracy of the present approach, numerical results for the static behavior of the FGM shell with perfectly bonded piezoelectric layers under thermomechanical boundary conditions are presented and compared with the results reported in Ref. [17, 19]. In this case, the material properties of the FGM host layer vary according to the power law function and $\chi_i^k=K_L=K_S=0$. Fig. 2 shows a good agreement for the distribution of temperature and radial stress with one reported in the literature. It is obvious from Fig. 2(b) that by increasing the number of grid points, the DQ method converges rapidly and approaches to the reported results.

In all examples to be considered, we assume $\chi_r^k=\chi_T^k=0$ to avoid the material penetration phenomenon [40, 41]. So, the hybrid shell with a uniform shear slip imperfection is considered. It is worth noting that the delamination problem of a hybrid cylindrical shell subjected to static normal tension loads, i.e. outward at the outer surface and inward at the inner surface, can be considered by taking $\chi_r^k\neq 0$ [42].

Table 1
Materials constants.

Property (GPa)	c_{11}	c_{12}	c_{13}	c_{22}	c_{23}	c_{33}	c_{55}
Sensor (PZT-4)	115	74	74	139	78	139	25.6
Actuator ($Ba_2NaNb_5O_{15}$)	135	52	5	247	104	239	66
Property*	e_{11}	e_{21}	e_{31}	e_{53}	$g_{11}\times10^{-9}$	$g_{33}\times10^{-9}$	$P_{11}\times10^{-5}$
Sensor (PZT-4)	15.1	-5.2	-5.2	12.7	5.6	6.5	5.4
Actuator ($Ba_2NaNb_5O_{15}$)	4.3	-0.3	-0.4	2.8	0.28	1.96	5.4
Property*	$\alpha_r\times10^{-6}$	$\alpha_\theta=\alpha_z$	$k_\theta=k_z$	k_r	$\mu_p\times10^{-7}$	ρ_p	
Sensor (PZT-4)	2.62	1.99×10^{-6}	2.1	2.5	4π	7500	
Actuator ($Ba_2NaNb_5O_{15}$)	2.45	4.39×10^{-6}	8.6	13.9	4π	5300	

* The units are: e in C/m^2, g in C^2/Nm^2, P_{11} in C^2/m^2K, α in 1/K, k in W/mK, μ in H/m and ρ in kg/m^3

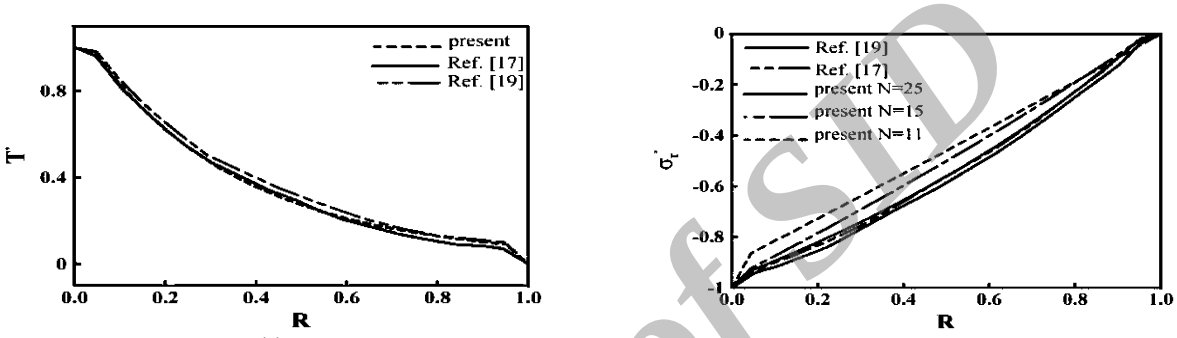

(a) (b)

Fig.2
Distribution of (a) temperature, (b) the radial stress.

To illustrate the influences of a magnetic field on the behavior of a smart cylindrical shell, the shell is placed in a constant magnetic field of $H=H^*\times2.23\times10^6$ *(A/m)*. The shell is considered to be subjected to an inner pressure $P_i=1$ *MPa* and we have: $T_i=5$, *V=100 v,* $\chi_z^k=K_L=K_S=0$. Fig. 3 shows effects of the magnetic field on the distribution of stresses and the radial displacement along the radial direction of the hybrid shell. Fig. 3(a) shows that by increasing the magnetic field, the curvature of the graph became inversed and the compressive radial stress is decreased significantly in most part of the shell. In contrast, the trend is vise versa near the inner surface. Fig. 3(b) shows that an increase in the magnetic field results in increasing the compressive hoop stress of FGM shell. According to Figs. 3(c) and (d), increasing the magnetic field has no significant effect on the longitudinal stress and transverse shear stress. Fig. 3(e) shows that the outward radial displacement decreases by increasing in the magnetic field. Whereas, more increase in the magnetic field results in inward radial displacement which increases by an increase in the magnetic field. Therefore, the radial displacement can be approximately vanished for a specific magnetic field. The magnitude of the Lorentz force depends on the magnitude of the magnetic field. In the pyroelectric materials there are an interaction between thermal, electric and mechanical field. Each of these fields can create stresses and displacements in the pyroelectric cylindrical shell. In addition, by existence of a magnetic field, the radial displacement results in creating the Lorentz force in the radial direction. Then, this force affects the stresses and displacements. It should be noted that by changing each of the effective parameters, the effect of Lorentz force on the behavior of smart structure may be changed.

Effects of the internal temperature (T_a) of the hybrid shell on stresses and the radial displacement are presented in Fig. 4. In this case, $H^*=80$ is considered and other parameters and conditions remain unchanged. It is observed from Fig. 4(a) that there are two points within the thickness of the hybrid shell that the radial stress is independent of the thermal loading applied on the inner surface. These two points are located at *R=0.1658* and *R=0.8719*. Between these two points, an increase in the applied thermal loading decreases the absolute value of the radial stress and the radial stress tends to be positive. Outside of these two points , however, the radial stress behavior is vise versa. Fig. 4(b) shows that by increasing the inner temperature the tensile hoop stress decreases and approximately vanishes. More increase in T_a leads to a compressive hoop stress. Moreover, the absolute value increases by increasing of the inner temperature. For a certain electro-magneto-thermo-mechanical condition , consequently, the hoop stress that is a key parameter in the crack growth can be approximately vanished. Furthermore, the difference between the hoop

stresses of pyroelectric layers consisted of FGM layer is increased by increasing the inner temperature. As shown in Fig. 4(c), there are two points within the thickness of the hybrid shell that the transverse shear stress is independent of the thermal loading applied on the inner surface. These two points are located at *R=0.1364* and *R=0.4813*. Between these two points, an increase in the applied thermal loading increases the positive transverse shear stress, where as outside of these two points the transverse shear stress exhibits a reverse behavior. The increase in the absolute value of the transverse shear stress in the outer surface of FGM layer is more significant than that of the inner surface. Besides, Fig. 4(d) shows that there existed a certain point *(R=0.3063)* at which the value of longitudinal stress shows no change while the thermal loading is changed. Before this point, an increase in the applied thermal loading increases the compressive longitudinal stress. After this point , in contrast, the longitudinal stress becomes tensile and rises by rising in T_a. It is shown that applying thermal loading leads to an increase in the tensile longitudinal stress in the outer surface as well as a compressive longitudinal stress in the inner surface of the FGM layer. This effect is more intensive in the outer surface. Fig. 4(e) shows that the positive radial displacement decreases by increasing the inner temperature and more increase in the inner temperature results in increasing the radial displacement in the opposite direction. So, there is a specific electro-magneto-thermo-mechanical condition wherein the radial displacement of the hybrid shell can be approximately close to the zero value.

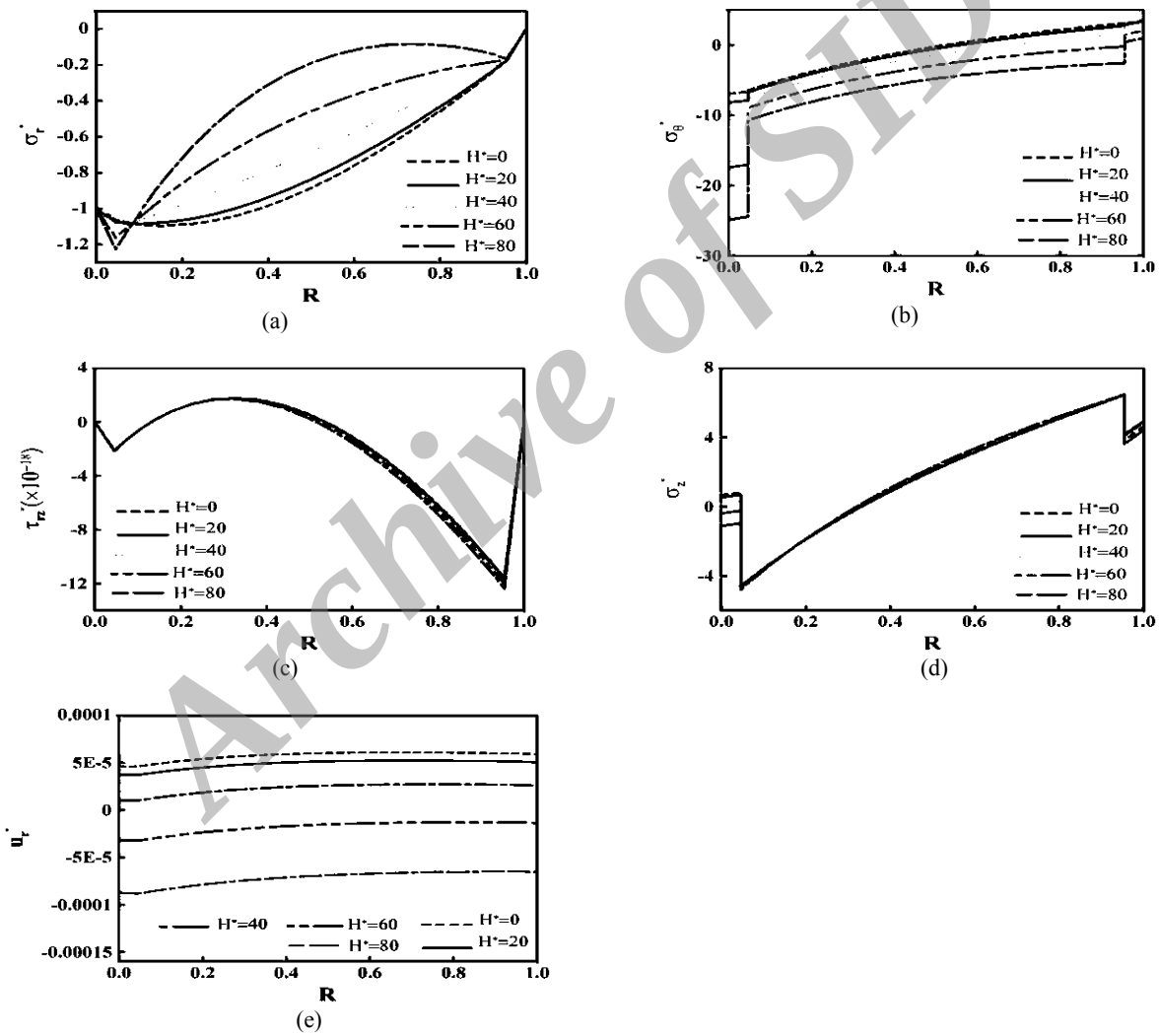

Fig.3
Distribution of (a) radial stress, (b) hoop stress, (c) transverse shear stress, (d) longitudinal stress, (e) radial displacement for different H^*.

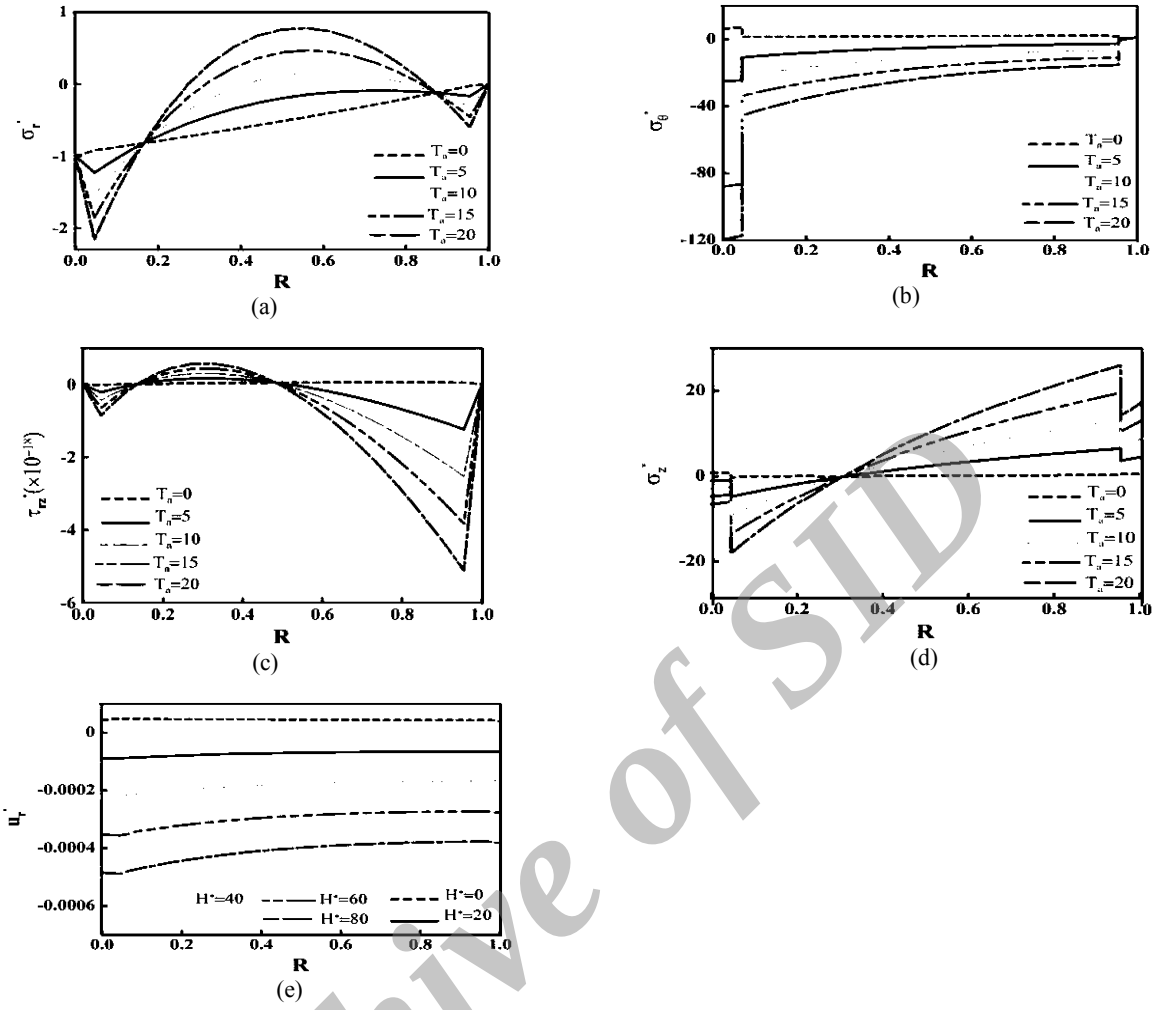

Fig.4
Distribution of (a) radial stress, (b) hoop stress, (c) transverse shear stress, (d) longitudinal stress, (e) radial displacement for different T_a.

The effect of the elastic foundation on the behavior of the hybrid shell is shown in Fig. 5. In this case: $P_i=1$ MPa, and other parameters remain unchanged $(K_S=k_S\times10^8,\ K_L=k_L\times10^8)$. Fig. 5(a) shows that an increase in the stiffness of the Winkler spring and shear layer of the elastic foundation results in an increase in the value of the radial stress in the outer surface of the shell. It is valuable to note that $k_L=k_S=0$ simulates the situation in which the shell is traction free on the outer surface. Fig. 5(b) shows that higher foundation stiffness leads to a slight decrease in the hoop stress of the hybrid shell. Regarding the inward radial displacement, the compressive hoop stress, and the reduction of this inward radial displacement by increasing in elastic stiffness, the decrease in the compressive hoop stress is reasonable. Fig. 5(c) depicts that the transverse shear stress experience no noticeable change by altering the foundation stiffness. More investigations show that by changing the elastic stiffness, the shear strain is not changed considerably. Thus, this is reasonable that the transverse shear stress experience no noticeable change with different elastic stiffness. Fig. 5(d) shows that the radial displacement decreases by increasing the stiffness of the elastic foundation. Regarding to Figs. 5(a) and (d), due to the inward radial displacement the presence of an elastic foundation helps to resist the radial displacement. This results in a tensile radial stress in the outer surface as well as a reduction in the radial displacement. It can be concluded that by changing the direction of the radial displacement, the elastic foundation shows a reverse effect on the behavior of the shell.

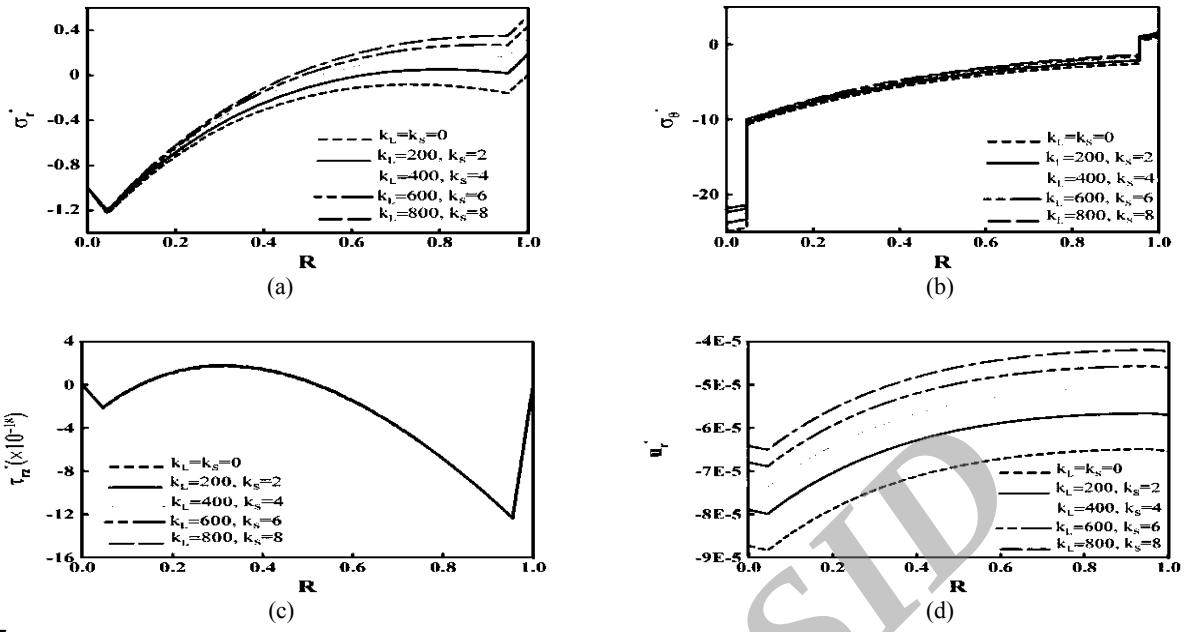

Fig.5
Distribution of (a) radial stress, (b) hoop stress, (c) transverse shear stress, (d) radial displacement for different k_L and k_S.

The effect of imperfection on stresses and displacements are listed in Table 2. and Fig. 6. In Table 2. , the magnitude of variables are declared at the middle point of the thickness and S is defined as: S=(middle radius)/(thickness of shell). Parameters and boundary conditions are like the previous one and $\chi_z^1=\chi_z^2=\chi\times10^{-10}$. As the compliance coefficient of the imperfection increases the absolute value of radial and hoop stresses are increased and the longitudinal stresses are decreased. For the case that the radial stress is tensile *(S=20)*, the radial stress decreases by increasing the compliance coefficient of the imperfection. The positive transverse shear stress increases and the minus transverse shear stress decreases by increasing the compliance coefficient of the imperfection. By increasing the compliance coefficient of the imperfection the longitudinal displacement decreases. However, the radial displacement shows a reverse behavior. Furthermore, as S increases the absolute values of hoop, longitudinal and transverse shear stresses as well as radial and longitudinal displacements are increased. However, the behavior of radial stresses is vice versa.

Fig. 7 shows the effect of the imperfect bonding on the sensor authority. In this case: $P_i=1KPa$, $H_0=0$, $V=100\ V$ and $T_0=0\ K$. As it is expected, the measured voltage in the sensor decreases by increasing the compliance coefficient of the imperfection. For large values of compliance coefficient of the imperfection, the curve becomes nearly flat representing no further significant change in the measured voltage.

The effect of the inhomogeneity index of FGM layer on the static response of the hybrid shell is shown in Fig. 8. In this case: the inner surface of FGM layer remain unchanged whereas $\eta=\eta_1=\eta_2=\eta_4$ and $P_i=1\ MPa$. Other parameters remain unchanged. According to Fig. 8, through-thickness distribution of stresses, displacement and temperature in the isotropic shells lay between the diagrams. Figs. 8(a)-(b) show that by changing the sign of the inhomogeneity index the curvature of graphs became vice versa. Altering the inhomogeneity index from a minus value to a positive value leads to an increase in the absolute value of the radial and hoop stresses. Fig. 8(c) shows that in the most part of the shell, increasing the inhomogeneity index from a minus value to a positive value leads to an increase in the positive value of the transverse shear stress in the middle part of the shell. However, it results in the minus value of the transverse shear stress in the inner and the outer surface of the FGM layer. Fig. 8(d) shows that by changing the sign of the inhomogeneity index the curvature of graphs became vice versa and increasing the inhomogeneity index results in an increase in the longitudinal stress. This increase is more significant in the outer surface of the FGM layer. Generally, it can be concluded from Figs. 8(a)-(d) that for the sake of decreasing the value of stresses at any point in the thickness direction it is necessary to use the FGM shell with a hard inner surface. Fig. 8(e) shows that the radial displacement decreases by decreasing in the inhomogeneity index. Fig 8(f) shows the distribution of the temperature in the hybrid shell. As it is observed, the direction of the curvature depends on the sign of the inhomogeneity index and an increase in the homogeneity index leads to an increase in the temperature of the point.

Table 2
Effect of imperfection on the static response of hybrid shell.

Entity	S	χ=0	χ=5	χ=10	χ=15	χ=20
σ_r^*	5	-0.19499	-0.21993	-0.23391	-0.24263	-0.24831
	10	-0.03945	-0.05281	-0.06076	-0.06845	-0.07533
	20	0.024135	0.016395	0.014591	-0.00915	-0.0077
σ_θ^*	5	-4.76751	-4.93437	-5.03325	-5.09918	-5.14688
	10	-8.23908	-8.41072	-8.55193	-8.65318	-8.73249
	20	-14.8276	-14.9877	-15.2002	-15.1241	-15.3111
σ_z^*	5	2.290138	1.791042	1.486702	1.283603	1.138754
	10	4.405712	3.882783	3.472729	3.144736	2.877753
	20	8.546134	7.993948	7.532758	7.094078	6.712753
$\tau_{rz}^*(\times10^{-19})$	5	2.68069	23.02767	33.69917	40.32056	44.62369
	10	-33.75967	-21.89417	-12.96661	-7.08783	-2.59358
	20	-51.18824	-44.87115	-42.31643	-35.29529	-31.17190
$u_r^*(\times10^{-4})$	5	-0.68830	-0.69087	-0.69177	-0.69240	-0.69308
	10	-3.70503	-3.71107	-3.71995	-3.72026	-3.71866
	20	-16.58073	-16.57166	-16.65656	-16.40878	-16.49310
$u_z^*(\times10^{-19})$	5	-0.22783	-0.21256	-0.20321	-0.19696	-0.19250
	10	-0.68076	-0.64843	-0.62317	-0.60274	-0.58607
	20	-2.21414	-2.14473	-2.08983	-2.02698	-1.98194

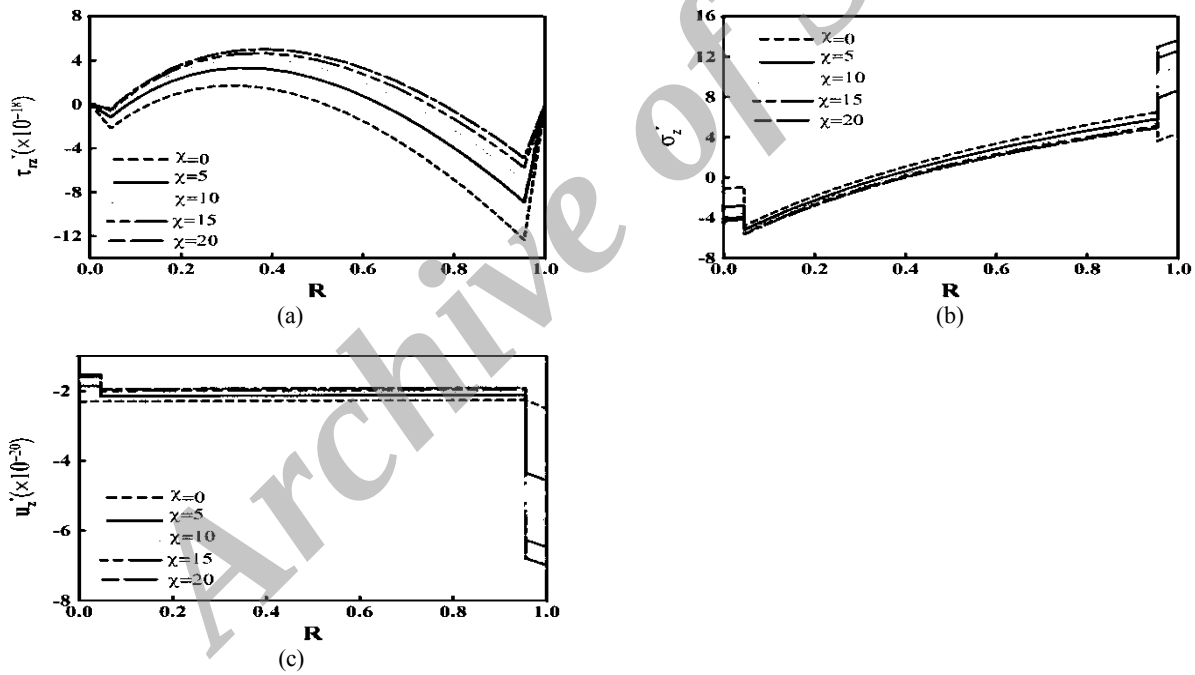

Fig.6
Distribution of (a) transverse shear stress, (b) longitudinal stress, (c) longitudinal displacement for different χ.

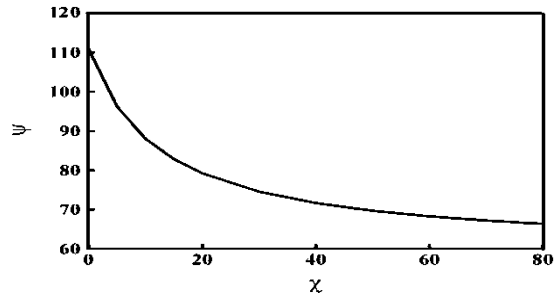

Fig.7
Influence of imperfect bonding on sensory potential.

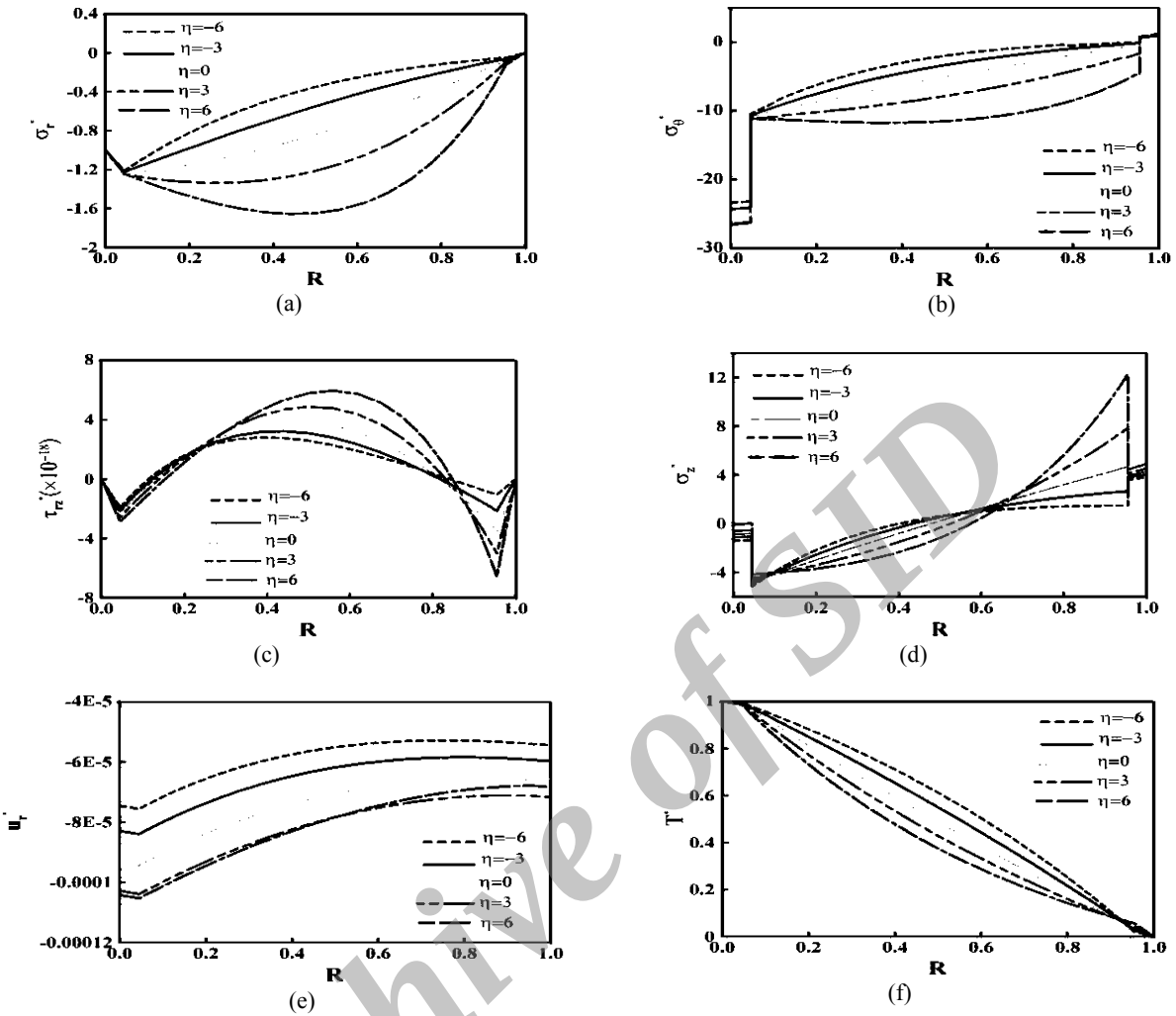

Fig.8
Distribution of (a) radial stress, (b) hoop stress, (c) transverse shear stress, (d) longitudinal stress, (e) radial displacement, (f) longitudinal displacement for different η.

Fig. 9 shows the distribution of stresses and radial displacement of the hybrid shell under different inner pressure. All of the parameters and conditions are as before. Fig. 9(a) shows that the radial stress in the points within the thickness is independent of the inner pressure. As it is observed, the compressive radial stress increases for higher inner pressure between these two points. However, for other parts this behavior is vise versa. This behavior shows that the effect of pyroelectric layer decreases for a higher inner pressure. Fig. 9(b) shows that the hoop stress of the FGM layer reduces for a higher inner pressure. It should be noted that this trend of stresses is just observed under the certain magnetothermomechanical boundary and environmental conditions. By eliminating the magnetic field or thermal field responses may be changed. Fig. 9(c) shows that a higher inner pressure leads to a reduction in the transverse shear stress of the hybrid shell. This reduction is more obvious near the outer surface of the FGM layer. Fig. 9(d) shows that the inward radial displacement (due to high magnetic field value) decreases by rising in the inner pressure. In fact, the graph of the radial displacement shifts upward by the inner pressure enhancement.

Fig. 10 depicts the effect of the aspect ratio of the shell (S) on the stresses and radial displacement distribution. Fig 10 shows that increasing S increases the hoop and transverse shear stresses as well as radial displacement. However, the radial stress exhibits a reverse behavior. It should be noted that this behavior is because of interaction of thermal, electric and mechanical fields as well as the effect of the magnetic field. In this mutiphysics analysis case, effects of the magnetic environment and thermal loading can overcome the effect of the mechanical loading in a thin shell.

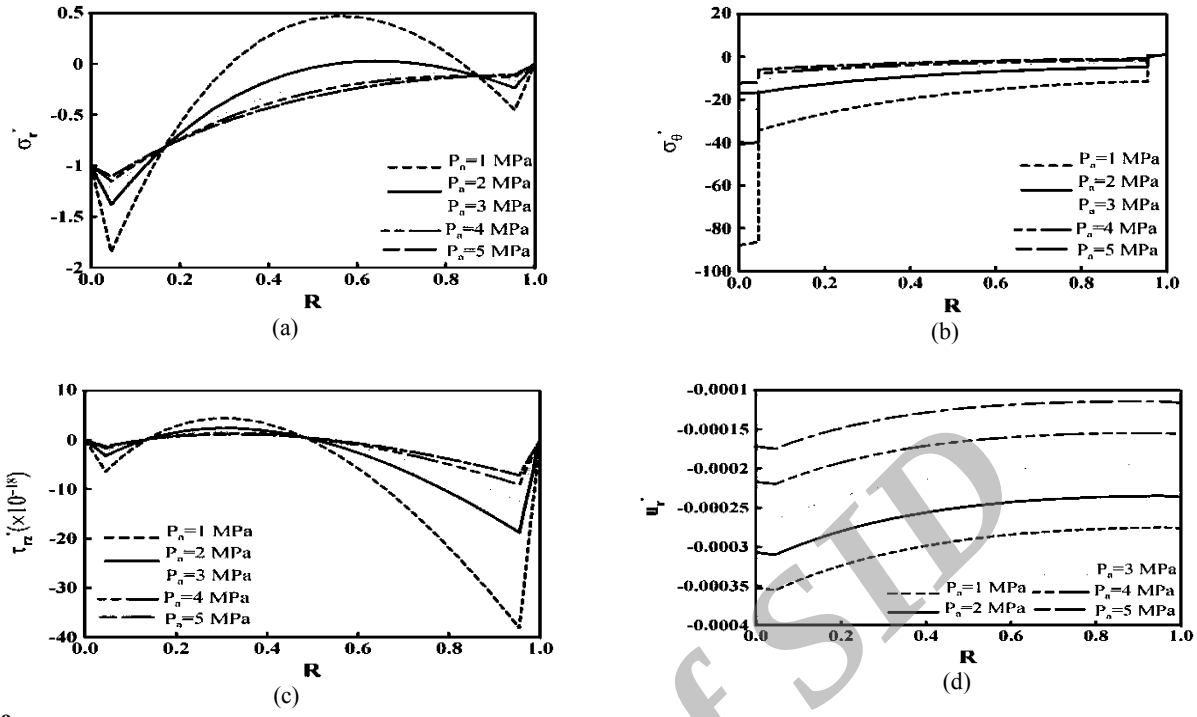

Fig.9
Distribution of (a) radial stress, (b) hoop stress, (c) transverse shear stress and (d) radial displacement for different P_a.

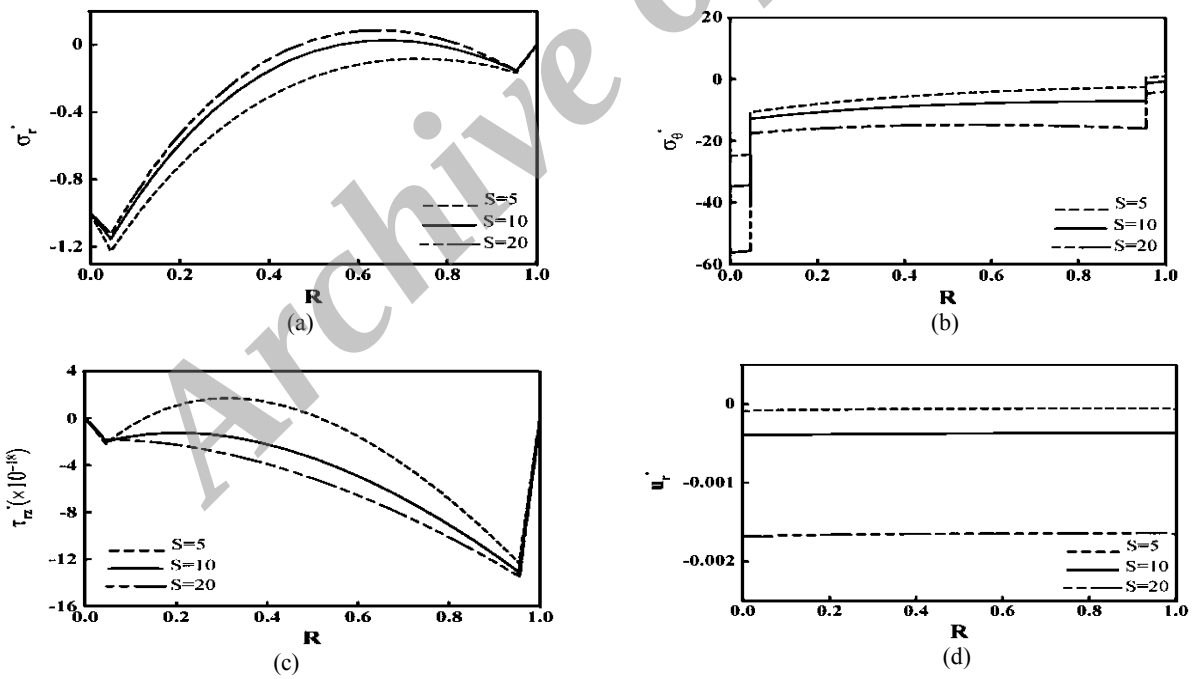

Fig.10
Distribution of (a) radial stress, (b) hoop stress, (c) transverse shear stress and (d) radial displacement for different S.

Fig. 11 illustrates the effect of the electric excitation of the actuator layer on the behavior of the hybrid shell. In this case, we have: P_i=100 Pa, T_i=0 and H^*=40. As is shown in Figs. 11(a) and (b), the radial stress near the inner surface of the FGM layer as well as radial displacement of the hybrid shell decrease by increasing in the electric excitation of the actuator layer. However, this reduction is more significant in the radial displacement. So, using

pyroelectric actuator layer an electric excitation is a way to reduce displacement and vibration of the FGM cylindrical shell.

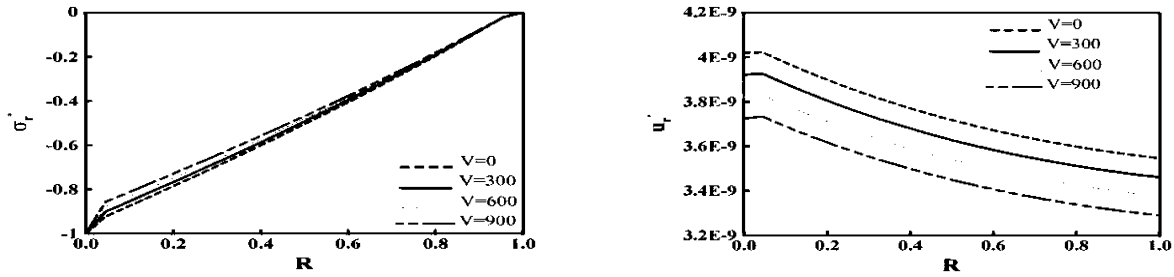

(a) (b)

Fig.11
Distribution of (a) radial stress, (b) radial displacement for different V**.**

5 CONCLUSION

A numerical solution for deformation of an exponentially graded hollow cylindrical shell with the inner and the outer surface imperfectly bonded pyroelectric layers and subjected to magneto-thermo-electro-mechanical loads is presented. The analysis was carried out by using a series type solution and DQ method. The numerical results are presented for sample problems and the following conclusions are obtained:

- By increasing the magnetic field, the radial stress decreases and the hoop stress increases. Besides, the radial displacement decreases and further increase results in changing the direction of the radial displacement. Therefore, the radial displacement can be vanished approximately for a specific magnetic field.
- Results show that there are some points within the thickness of the shell at which the radial, longitudinal and transverse shear stresses are independent of the thermal loading. Furthermore, for a certain electro-magneto-thermo-mechanical condition the hoop stress can be vanished approximately. There is a specific thermal condition wherein the radial displacement can be approximately close to the zero value.
- By an increase in the stiffness of the elastic foundation, the radial displacement decreases and the value of the radial stress in the outer surface of the shell alters proportional to the direction of the radial displacement.
- As the compliance coefficient of the imperfection increases, the absolute value of the radial displacement as well as radial and hoop stresses are increased. However, the longitudinal stress and the longitudinal displacement decreased. The measured voltage in the sensor decreases by increasing the compliance coefficient of the imperfection.
- Increasing the inhomogeneity index leads to an increase in the absolute value of radial and hoop stresses as well as the radial displacement. It is observed that for the sake of decreasing the value of stresses at any point in the thickness direction it is necessary to use the FGM shell with a hard inner surface.

REFERENCES

[1] Ghorbanpour Arani A., Amir S., 2011, Magneto-thermo-elastic stresses and perturbation of magnetic field vector in a thin functionally graded rotating disk, *Journal of Solid Mechanics* **3** (4): 392-407.

[2] Ghorbanpour Arani A., Golabi S., Saadatfar M., 2006, Stress and electric potential fields in piezoelectric smart spheres, *Journal of Mechanical Science and Technology* **20**: 1920-1933.

[3] Saadatfar M., Razavi S.A., 2009, Piezoelectric hollow cylinder with thermal gradient, *Journal of Mechanical Science and Technology* **23**: 47-55.

[4] Saadatfar M., Rastgoo A., 2008, Stress in piezoelectric hollow sphere with thermal gradient, *Journal of Mechanical Science and Technology* **22**: 1460-1467.

[5] Shariyat M., 2009, Dynamic buckling of imperfect laminated plates with piezoelectric sensors and actuators subjected to thermo-electro-mechanical loadings, considering the temperature-dependency of the material properties, *Composite Structures* **88** (2): 228-239.

[6] Shariyat M., 2008, Dynamic buckling of suddenly loaded imperfect hybrid FGM cylindrical shells with temperature-dependent material properties under thermo-electro-mechanical loads, *International Journal of Mechanical Sciences* **50** (12): 1561-1571.

[7] Shariyat M., 2009, Vibration and dynamic buckling control of imperfect hybrid FGM plates with temperature-dependent material properties subjected to thermo-electro-mechanical loading conditions, *Composite Structures* **88** (2): 240-252.

[8] Ebrahimi F., Rastgoo A., 2009, Temperature effects on nonlinear vibration of FGM plates coupled with piezoelectric actuators, *Journal of Solid Mechanics* **1** (4): 260-364.

[9] Rastgo ghamsari A., Ebrahimi F., 2008, Free vibration analysis of smart annular FGM plates integrated with piezoelectric layers, *Smart Materials and Structures* **17**: 015044.

[10] Ebrahimi F., Rastgo ghamsari A., 2008, FSDPT based study for vibration analysis of piezoelectric coupled annular FGM plate, *Journal of Mechanical Science and Technology* **23**: 2157-2168.

[11] Jabbari M., Farzaneh Joubaneh E., Khorshidvand A.R., Eslami M.R., 2013, Buckling analysis of porous circular plate with piezoelectric actuator layers under uniform radial compression, *International Journal of Mechanical Sciences* **70**: 50-56.

[12] Khorshidvand A.R., Jabbari M., Eslami M.R., 2012, Thermoelastic buckling analysis of functionally graded circular plates integrated with piezoelectric layers, *Journal of Thermal Stresses* **35**: 695-717.

[13] Khorshidvand A.R., Farzaneh Joubaneh E., Jabbari M., Eslami M.R., 2014, Buckling analysis of a porous circular plate with piezoelectric sensor–actuator layers under uniform radial compression, *Acta Mechanica* **225**: 179-193.

[14] Saadatfar M., Aghaie-Khafri M., 2014, Hygrothermosmagnetoelectroelastic analysis of a functionally graded magnetoelectroelastic hollow sphere resting on an elastic foundation, *Smart Materials and Structures* **23**: 035004.

[15] Alibeigloo A., Nouri V., 2010, Static analysis of functionally graded cylindrical shell with piezoelectric layers using differential quadrature method, *Composite Structures* **92**: 1775-1785.

[16] Alibeigloo A., Kani A.M., Pashaei M.H., 2012, Elasticity solution for the free vibration analysis of functionally graded cylindrical shell bonded to thin piezoelectric layers, *International Journal of Pressure Vessels and Piping* **89**: 98-111.

[17] Alibeigloo A., 2011, Thermoelastic solution for static deformations of functionally graded cylindrical shell bonded to thin piezoelectric layers, *Composite Structures* **93**: 961-972.

[18] Alibeigloo A., 2011, Exact solution of an FGM cylindrical panel integrated with sensor and actuator layers under thermomechanical load, *Smart Materials and Structures* **20**: 035002.

[19] Akbari Alashti R., Khorsand M., 2011, Three-dimensional thermo-elastic analysis of a functionally graded cylindrical shell with piezoelectric layers by differential quadrature method, *International Journal of Pressure Vessels and Piping* **88**: 167-80.

[20] Akbari Alashti R., Khorsand M., 2012, Three-dimensional dynamo-thermo-elastic analysis of a functionally graded cylindrical shell with piezoelectric layers by DQ-FD coupled, *International Journal of Pressure Vessels and Piping* **96**: 49-67.

[21] Ghorbanpour Arani A.G., Salari M., Khademizadeh H., Arefmanesh A., 2009, Magnetothermoelastic transient response of a functionally graded thick hollow sphere subjected to magnetic and thermoelastic fields, *Archive of Applied Mechanics* **79** (6-7): 481-497.

[22] Ghorbanpour Arani A., Bakhtiari R., Mohammadimehr R., Mozdianfard M.R., 2001, Electro-magneto-mechanical responses of a radially polarized rotating functionally graded piezoelectric shaft, *Turkish Journal of Engineering and Environmental Sciences* **36** (1): 33-44.

[23] Ghorbanpour Arani A., Kolahchi R., Mosallaie Barzoki A.A., 2011, Effect of material in-homogeneity on electro-thermo-mechanical behaviors of functionally graded piezoelectric rotating shaft, *Applied Mathematical Modelling* **35** (6): 2771-2789.

[24] Kong T., Li D.X., Wang X., 2009, Thermo-magneto-dynamic stresses and perturbation of magnetic field vector in a non-homogeneous hollow cylinder, *Applied Mathematical Modelling* **33**: 2939-2950.

[25] Khalili S.M.R., Mohazzab A.H., Jabbari M., 2009, Analysis on centrifugal load effect in FG hollow sphere subjected to magnetic field, *Journal of Solid Mechanics* **1**: 300-312.

[26] Dai H.L., Hong L., Fu Y.M., Xiao X., 2010, Analytical solution for electro-magneto-thermo-elastic behaviors of a functionally graded piezoelectric hollow cylinder, *Applied Mathematical Modelling* **34**: 343-357.

[27] Shariyat M., Asemi K., 2014, Three-dimensional non-linear elasticity-based 3D cubic B-spline finite element shear buckling analysis of rectangular orthotropic FGM plates surrounded by elastic foundations, *Composites Part B: Engineering* **56**: 934-947.

[28] Shariyat M., Mohammadjani R., 2013, Three-dimensional stress field analysis of rotating thick bidirectional functionally graded axisymmetric annular plates with nonuniform loads and elastic foundations, *Journal of Composite Materials* **48**: 2879-2904.

[29] Shariyat M., Alipour M.M., 2011, Differential transform vibration and modal stress analyses of circular plates made of two-directional functionally graded materials resting on elastic foundations, *Archive of Applied Mechanics* **81**: 1289-1306.
[30] Shariyat M., Alipour M.M., 2013, A power series solution for vibration and complex modal stress analyses of variable thickness viscoelastic two-directional FGM circular plates on elastic foundations, *Applied Mathematical Modelling* **37**: 3063-3076.
[31] Shariyat M., Jafari R., 2013, A micromechanical approach for semi-analytical low-velocity impact analysis of a bidirectional functionally graded circular plate resting on an elastic foundation, *Meccanica* **48**: 2127-2148.
[32] Alipour M.M., Shariyat M., A power series solution for free vibration of variable thickness mindlin circular plates with two-directional material heterogeneity and elastic foundations, *Journal of Solid Mechanics* **3** :183-197.
[33] Ghorbanpour Arani A., Kolahchi R., Mosallaie Barzoki A.A., Mozdianfard M.R., Noudeh Farahani M., 2012, Elastic foundation effect on nonlinear thermo-vibration of embedded double-layered orthotropic grapheme sheets using differential quadrature method, *Journal of Mechanical Engineering Science* **227**(4): 862-879.
[34] Saadatfar M., Aghaie-Khafri M., 2014, Electromagnetothermoelastic behavior of a rotating imperfect hybrid functionally graded hollow cylinder resting on an elastic foundation, *Smart Structures and Systems*, in press.
[35] John D.K., 1984, *Electromagnetics*, McGraw-Hill, Inc, New York.
[36] Kiani Y., Akbarzadeh A.H., Chen Z.T., Eslami M.R., 2012, Static and dynamic analysis of an FGM doubly curved panel resting on the Pasternak-type elastic foundation, *Composite Structure* **94**: 2474-2484.
[37] Kapuria S., Nair P.G., 2010, Exact three-dimensional piezothermoelasticity solution for dynamics of rectangular cross-ply hybrid plates featuring interlaminar bonding imperfections, *Composite Science and Technology* **70**: 752-762.
[38] Shu C., 2000, *Differential Quadrature and its Application in Engineering*, New York, Springer Publication.
[39] Chen W.Q., Bian Z.G., Lv C.F., 2004, 3D free vibration analysis of a functionally graded piezoelectric hollow cylinder filled with compressible fluid, *International Journal of Solids and Structures* **41**: 947-964.
[40] Cheng Z.Q., Jemah A.K., Williams F.W., 1996, Theory for multilayered anisotropic plates with weakened interfaces, *Journal of Applied Mechanic* **63**: 1019-1026.
[41] Cheng Z.Q., Kennedy D., Williams F.W., 1996, Effect of interfacial imperfection on buckling and bending behavior of composite laminates, *AIAA Journal* **34**: 2590-2595.
[42] Shu X.P., Soldatos K.P., 2001, An accurate delamination model for weakly bonded laminates subjected to different sets of edge boundary conditions, *International Journal of Mechanical Science* **43**: 935-959.